

Chilldown Simulation for the Hydrogen Branch of a Cryogenic Upper Stage Rocket Using a Numerically Generated Performance Map for the Turbopump

Marius C. Banica and Menko Wisse***

**Astrium Space Transportation*

66, Route de Verneuil, 78133 Les Mureaux CEDEX, France

***Astrium Space Transportation*

Airbus Allee 1, 28199 Bremen, Germany

06.07.2011

Abstract

The propellant feed valves of a cryogenic rocket engine are usually opened some time before ignition to allow cold propellants to enter the engine feed system and reduce its temperature. This process is commonly known as chilldown. Numerical studies can support its optimization but often suffer from modeling difficulties and excessive runtimes. We partly circumvent these disadvantages by geometrically simplifying the fuel pump and using a CFD method to generate its chilldown performance map. In a second step, the map is used in a system simulation for a real upper stage and the predictions are compared with flight data.

1. Introduction

For cryogenic rockets, chilldown is an essential prerequisite for the prevention of turbopump cavitation. The process is generally initiated by a premature opening of the tank valves. The propellants then enter the initially hot feeding system, where they evaporate quickly. The latent heat of evaporation removes heat from the system components and this leads to a local pressure rise that limits mass flow rates. Local vapour generation ceases when the temperatures drop below the saturation temperature. The end of the chilldown process is reached when the propellant temperatures stabilize within a pre-defined bandwidth that is determined by the operating requirements of the engine. Since the heated fluids are expelled into vacuum, process optimization is imperative to limit propellant loss. Some analyses of entire feeding systems were carried out as part of the Apollo moon program, see e.g. Davisson and McHarris [1]. However, analyses of simpler systems, such as single vertical or horizontal tubes, are more prevalent in the open literature. Examples include the recent work by Yuan et al. [2, 3] and Kawanami et al. [4, 5] while Carey [6] provides an exhaustive overview on the topic. The scarcity of published feed system chilldown studies might be linked to the inherent complexity in modeling convective phase-change processes. For example, present numerical methods usually rely on empirical or semi-empirical relations, rather than rigorous analytical analysis. These methods can still be helpful, however, when the primary aim is not to describe the chilldown process in every detail but rather to obtain general trends, improve system understanding and achieve process optimization. Several approaches exist. On a high-fidelity level, computational fluid dynamics (CFD) provides enhanced insights into the involved physics but on larger scales the approach often entails long runtimes. Simplified system models, on the other hand, reduce runtimes but cannot describe complex three dimensional flow patterns or geometries. This leads to problems in accounting for the fuel pumps, which often represent the major heat sinks in the system. In an attempt to combine the respective advantages of CFD and lower fidelity system models, we use a combination of both to obtain an adequate system description. The resulting method constitutes an engineering solution where the target is to quickly estimate propellant use, chilldown times and evaluate system behavior. Our procedure is as follows:

1. The cryogenic fuel pumps are simplified as axisymmetric structures. Their thermal behavior is then analyzed by means of state-of-the-art multiphase CFD simulations. Through adequate parameter variations, pump per-

formance maps can be developed. These can be formulated in a general manner and describe the heat transfer characteristics of the pump as a function of various initial and boundary conditions.

2. A numerical model of the hydrogen feeding system of a real liquid hydrogen-liquid oxygen (LH2-LOX) rocket engine is considered. In the model, the pump is represented by its performance maps.
3. The feed system behavior is analyzed and the model validated through comparisons with flight data. The latter include temperature and pressure histories at various locations as well as estimates of propellant consumption.

The focus of this study is on the ascent phase of the vehicle. Re-ignition after an extended coasting phase is not considered. However, the method can, in principle, be extended to cover such scenarios.

2. Preliminary Considerations

2.1 Relevant Forces

The relevant physical phenomena can be classified according to their importance. For this purpose, it is helpful to consider the relative sizes of the inertial forces (IN), viscous forces (VF), buoyancy forces (BY), body forces (BF) and surface tension (ST). Their possible ratios yield the Reynolds number, Re , the Weber number, We , the Bond number, Bo , the Grashof number, Gr , the capillary number, Ca , and combinations thereof. Present value ranges for several variables and material properties are given in table 1, where ΔT , σ and D are preliminary estimates. This data is used to calculate the force ratios from table 2, where the column heads and row heads indicate the denominators and nominators, respectively. We observe that the force ratios vary over a wide range. For small droplet diameters, ST can be of the same order of magnitude or larger than IN and for large droplet diameters, BY are of the order of magnitude of IN. BF and VF are small throughout but the former are dominant in the boundary layers. This is accounted for by introducing stagnation pressure losses in the system model and calculating the boundary layers in the CFD simulation. The data illustrates the difficulties in choosing one modeling approach that can represent all relevant phenomena while maintaining sensible computation times. As a first estimate, therefore, ST, BY and BF are neglected. This means that the droplet diameters are assumed to lie in the medium of the range indicated in table 1.

Table 1: Value ranges for relevant variables and material properties

Variable	Value	Unit	Description
u	0.3-2.5	[m/s]	Flow velocity
L	0.0568	[m]	Reference length
D	$10^{-4} - 10^{-3}$	[m]	Bubble diameter
a	10-35	[m/s ²]	Acceleration
T	25-270	[K]	Fluid temperature
ΔT	10-20	[K]	Local temperature difference in fluid
ρ	0.2-70	[kg/m ³]	Density
σ	0.01-0.05	[N/m]	Surface tension
β	$= 1/T$	[1/K]	Thermal expansion coefficient
μ	$7.9 - 9.4 \cdot 10^{-6}$	[Pas]	Molecular viscosity

2.2 Heat Transfer Mechanisms

The propellant feed system mainly consists of pipes. Here, heat is transferred from the hot walls to the cool fluids through conduction, convection, phase change and radiation. Several flow regimes can be distinguished. For a given fluid, their appearance largely depends on the wall temperature, T_w . For liquids and wall temperatures smaller than the limit for the onset of nucleate boiling, i.e. $T_w < T_{ONB}$, and for superheated vapor, no phase change occurs and only single-phase heat transfer exists. For liquids and $T_w \geq T_{ONB}$, nucleate boiling is observed. This state is associated with bubble generation at nucleation sites on the walls and a significant increase in heat transfer rates when compared to single-phase flow. The bubbles are convectively transported by the liquid. With increasing downstream distance, the gas mass fraction, Y_g , increases. For $Y_g > 0.7$ the regime of mist flow evaporation begins. Here, liquid is convectively transported as dispersed bubbles and the liquid film on the wall has dried out. For sufficiently large downstream

Table 2: Ratio of forces in the chilldown process, column heads indicate denominators, row heads indicate nominators

	IN	VF	BY	BF	ST
IN	1	$10^{-3} - 10^{-5}$	$10^{-7} - 10^0$	$10^{-3} - 10^{-2}$	$10^{-1} - 10^5$
VF	$\frac{10^3 - 10^5}{Re}$	1	$10^{-5} - 10^4$	$10^2 - 10^3$	$10^2 - 10^{10}$
BY	$\frac{10^0 - 10^7}{Re/Gr}$	$\frac{10^{-4} - 10^5}{1/Gr}$	1	$10^{-3} - 10^7$	$10^{-2} - 10^{13}$
BF	$\frac{10^2 - 10^3}{We/Bo}$	$\frac{10^{-3} - 10^{-2}}{We/BoRe}$	$\frac{10^{-7} - 10^3}{GrCa/Bo}$	1	$10^1 - 10^7$
ST	$\frac{10^{-5} - 10^1}{We}$	$\frac{10^{-10} - 10^{-2}}{Ca}$	$\frac{10^{-13} - 10^2}{GrCa}$	$\frac{10^{-7} - 10^{-1}}{Bo}$	1

distances the entire liquid is evaporated and only vapour remains. For still larger wall temperatures, i.e. $T_w > T_{DNB} > T_{ONB}$, the flow pattern changes and gas layers begin to form between the wall and the liquid. The point of change is referred to as the departure from nucleate boiling (DNB) and the new flow state is called transition boiling. Here, the heat transfer rates significantly decrease with only small increases in T_w . Eventually, with rising T_w , transition boiling is passed, and the regime of film boiling is reached. Flows of this type are characterized by vapor layers that form between the inner liquid core and the wall, thus isolating the liquid. Heat transfer rates are dramatically reduced when compared to nucleate boiling. The various flow regimes can be tracked on a flow map, such as the one presented by Taitel and Dukler [7]. Several correlations exist to describe heat transfer rates for nucleate boiling but the available data on transition boiling and film boiling is more scarce. An overview is given by Carey [6], among others. Furthermore, the implementation of such correlations in a numerical code can lead to instabilities. Recent attempts at implementing a unified approach that includes all flow regimes were made by e.g. Yuan et al. [2] and Kawanami et al. [4]. In literature, boiling in horizontal or vertical tubes is usually considered and either constant wall temperatures or constant wall heat fluxes are applied. As a secondary heat transfer mechanism, radiation from the pipe outer surfaces to the environment can be accounted for. In the present case, the feed lines are subject to time dependent wall temperatures, wall heat fluxes and acceleration states and have various orientations in space.

3. Numerical Methods

3.1 CFD Code

We use the commercial code Fluent v12.0 for the fuel pump simulations. The code is described in detail in the appropriate handbooks and so only a short overview is given here. The governing equations are solved in their axisymmetric form in a finite volume formulation using quadrilateral elements. The convective fluxes are discretized by a formally third order MUSCL scheme and the diffusive fluxes by formally second order central differences. The solution is advanced in time by an implicit time integration scheme with a constant time step of $\Delta t = 0.001 s$. Boundary layers are approximated by wall functions while ensuring their range of validity is maintained. Turbulence is modeled by the realizable $k\epsilon$ model. The multiphase flow is described by a mixture model, where the phases are assumed to be completely dispersed. A transport equation is solved for each phase and the phases can move at different speeds. This approach is applicable in cases where the gas phase is thoroughly mixed with the liquid phase, which is assumed to be true for the current situation. In addition, it was shown in section 2.1 that ST are negligible, which further justifies the choice. Alternatives include methods where the phase boundaries are locally reconstructed but this often leads to excessive runtimes. Other alternatives are Euler-Lagrange methods that are based on tracking particles, e.g. gas bubbles, through the flow. These methods are applicable for low gas volume fractions α . Here, however, $0 \leq \alpha \leq 1$.

3.2 System Simulation

The commercial code EcosimPro is used for the system analysis together with the ESPSS libraries. Both are described in detail in the appropriate handbooks and hence only a brief overview is provided here. The method is based on breaking down complex systems into their subcomponents. Each component is then described by a set of governing

equations. The components are linked by requiring some variables to be equal at the component interfaces. Mathematically, this leads to a set of discretized coupled non-linear equations for the present problem. They are advanced in time by a formally second order implicit time integration scheme. The system consists of lines, valves, thrusters, junctions and adiabatic volumes. The governing equations are the Navier-Stokes equations in one-dimensional form. They are discretized in space by a formally second order finite volume method. Artificial dissipation is added for stability. Stagnation pressure losses in the components are calculated based on the data provided by Idel'cik [8]. Heat conduction in the walls is assumed to be purely radial, i.e. axial and circumferential heat fluxes are neglected. In the tank, heat transfer between the ullage and the tank walls is modelled as heat transfer with a vertical wall. Heat transfer between the phases is modelled as heat transfer with a horizontal plate. Mass transfer between the phases is modelled according to [9]. Radiative heat transfer to the environment is accounted for by the Stefan-Boltzmann law and the pipes are assumed to radiate into free space. Radiation inside the lines is neglected. Single phase heat transfer ($Y_g = 0$ and $Y_g > 0.99$) is modelled with the Dittus-Boelter relation. Nucleate boiling for $Y_g < 0.7$ is modelled using the correlation of Chen [10]. Mist flow evaporation for $0.9 < Y_g < 0.99$ is modelled using the correlation of Dougall and Rohsenow [11]. For $0.7 \leq Y_g \leq 0.9$, a cubic spline interpolation between these correlations is used. Film boiling is ignored.

4. Fuel Pump

4.1 Numerical Model

The numerical model of the hydrogen fuel pump is shown in figure 1. The geometry is axisymmetric with respect to the indicated axis. It is discretized by 3088 quadrilateral elements in the fluid and 4840 quadrilateral elements in the solids. The inflow is parallel to the axis of symmetry and the outflow is radial. At the inflow, turbulence levels are set to 5%, the static temperature is set to the saturation temperature $T_{LH2,pi} = 25.415K$ and the velocity and vapor mass fraction are systematically varied. At the outlet, the static pressure is set to $p_{LH2,po} = 3.5 \cdot 10^5 Pa$. The starting solution for the unsteady runs is a steady state solution for constant wall temperatures. The inflow velocity, v_{pi} , and the inflow void fraction, α_{pi} , are varied systematically to change Re and Pr within the ranges expected in practice.

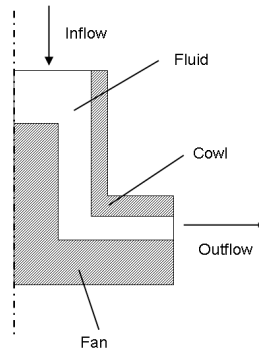


Figure 1: Simplified hydrogen turbopump model for the numerical simulations

4.2 Non-Dimensional Variables and Chillover Curves

Except for the pump bearing temperature, T_B , all time dependent temperatures, T , are written as

$$\Theta = \frac{T - T_{LH2}}{T_{init} - T_{LH2}}, \quad (1)$$

where T_{LH2} is the LH2 temperature in the tank, T_{init} is the initial component temperature and $\Theta \in [0; 1]$. For T_B , the following normalization is more advantageous

$$\Theta_B = \frac{T_B}{T_c}, \quad (2)$$

where T_c is the critical temperature above which pump operation is considered unsafe. The mass averaged temperature in the pump can be calculated from

$$T_m = \frac{1}{m_{pump}} \int_{pump} \rho T dV, \quad (3)$$

where m_{pump} is the pump mass, ρ is the pump material density, T is the local pump temperature and, using relation (1), $\Theta_m = \Theta(T_m)$. Pressures are normalized with the initial tank ullage pressure for the mean case (see section 6.2) according to

$$\tilde{p} = \frac{P}{P_{ull,mean\ case}^{t=0}} \quad (4)$$

Consumed masses, Δm , are normalized with the consumed mass for the mean case (see section 6.2) $\Delta \tilde{m} = \Delta m / \Delta m_{mean\ case}$. Nu for the pump is calculated from

$$Nu = \frac{\dot{q}D}{\lambda A(T_m - T_{LH2})}, \quad (5)$$

where \dot{q} is the heat flux, D is the pump inflow diameter, λ is the fluid thermal conductivity fluid and A is the total surface area of heat exchange. The chilldown curves are generated by systematically varying 1) v_{pi} (i.e. Re), and 2) α_{pi} (i.e. Pr). Here, the pump thermal behaviour is adequately described by $Nu(\Theta, Re, Pr)$ and $\partial T_m(\Theta, Re, Pr)/\partial t$. Together, these variables can be used to construct the pump performance maps if they are written in matrix form as $\mathbf{Nu}, \mathbf{T} \in \mathbb{R}^3$. However, the matrix dimensions and hence the computational effort can be reduced by correlating the numerical data with

$$\frac{Nu}{Re^{x(Pr)}} \quad \text{and} \quad \frac{1}{Re^{w(Pr)}} \frac{\partial T_m}{\partial t}, \quad (6)$$

where $w = 0.75$ provided acceptable results and the function $x(Pr)$ was found numerically. The construction of the performance maps is discussed further in section 4.3 below. Figure 2 (a) shows an example for $Nu(\Theta_m)$ for the case $\alpha = 0$, $x = 0.75$ and several different Re , using relation (6). The curves show an acceptable overlap over much of the range but differences can be observed for medium Θ_m . Similar data are shown in Figure 2 (b) for $\alpha = 1$, $x = 0.86$. The range of Re is different here since the fluid is now purely gaseous. The curves overlap satisfactorily, which indicates that the correlation is valid in this Re range. Figure 2 (c) shows $\partial T_m/\partial t(\Theta_m)$ for $\alpha = 0$, $w = 0.75$, using (6). The curve overlaps are largely acceptable, except for high Θ_m , where there are notable differences. Similar data is shown in 2 (c) for $\alpha = 1$, $w = 0.75$. The overlap here is better but differences remain at larger Θ_m . Note that, for brevity, figure 2 shows only a few examples for α but for $0 \leq \alpha \leq 1$ the situation is similar.

4.3 Construction of the Performance Maps

Based on the discussion above and using the numerically generated results for the chilldown curves, the performance maps can be calculated from

$$\mathbf{Nu}^{m \times l} = \begin{pmatrix} Pr_1 & \dots & \dots & Pr_l \\ \Theta_1 & \frac{Nu}{Re^{x(\alpha_1)}}(Pr_1, \Theta_1) & \dots & \dots & \frac{Nu}{Re^{x(\alpha_l)}}(Pr_l, \Theta_1) \\ \vdots & \vdots & \ddots & \vdots & \\ \Theta_m & \frac{Nu}{Re^{x(\alpha_1)}}(Pr_1, \Theta_m) & \dots & \dots & \frac{Nu}{Re^{x(\alpha_l)}}(Pr_l, \Theta_m) \end{pmatrix} \quad (7)$$

$$\mathbf{T}^{m \times l} = \begin{pmatrix} Pr_1 & \dots & \dots & Pr_l \\ \Theta_1 & \frac{1}{Re^{w(\alpha_1)}} \frac{\partial T_{avg}}{\partial t}(Pr_1, \Theta_1) & \dots & \dots & \frac{Nu}{Re^{x(\alpha_l)}}(Pr_l, \Theta_1) \\ \vdots & \vdots & \ddots & \vdots & \\ \Theta_m & \frac{Nu}{Re^{x(\alpha_1)}}(Pr_1, \Theta_m) & \dots & \dots & \frac{Nu}{Re^{x(\alpha_l)}}(Pr_l, \Theta_m) \end{pmatrix}. \quad (8)$$

In practice, the system simulation starts from predefined initial conditions. Using relation (5), the heat flux and the instantaneous change in pump temperature are then calculated from equations (7) and (8), respectively. The heat flux is used as a source term in the energy equation of the pump component. The above relations show that at least l calculations are needed to generate the performance maps for constant Re while $x(\alpha)$ is calculated by systematically varying Re . The generation of (7) and (8) hence requires some computational effort. However, the maps only have to be generated once for each geometry and can subsequently be expanded to include e.g. the influence of the acceleration state of the system and other dependencies. In principle, the pump also introduces a stagnation pressure loss into the system. However, from the CFD solution, this loss was estimated to be small compared to the other losses in the system and was hence neglected.

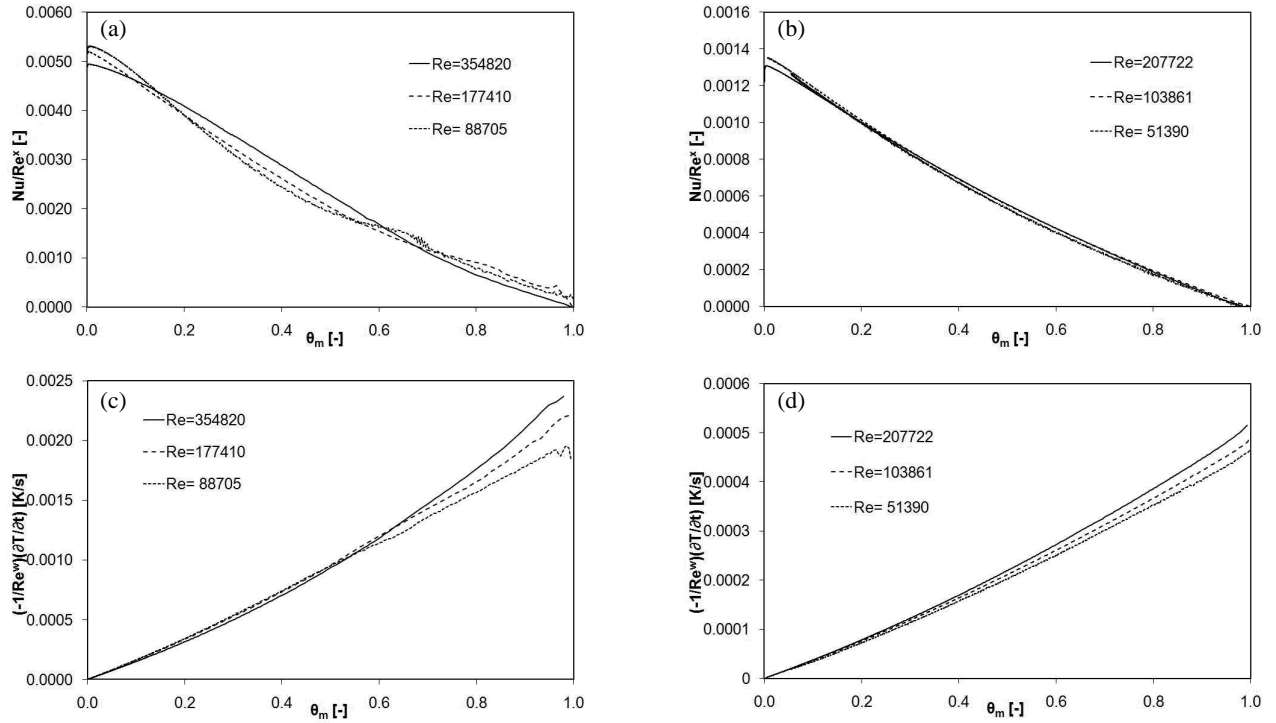


Figure 2: Nu as a function of Θ_m for various Re for (a) $x = 0.75$, $\alpha = 0$ and (b) $x = 0.86$, $\alpha = 1$; $\partial T_m / \partial t$ as a function of Θ_m for various Re and (c) $w = 0.75$, $\alpha = 0$ and (d) $w = 0.75$, $\alpha = 1$; v is the pump inflow velocity

5. Feed System

5.1 Architecture

The present method is validated against flight data for the hydrogen side of the propellant feed system of the Ariane 5 upper stage ESC-A and its HM7B engine. The engine uses LH2 and LOX as propellants. The stage feeding system is schematically shown in figure 3 (a). The relevant lines are denoted by marked as Lx with $x=1\dots 8$. Lengths are not drawn to scale. The relevant valves are the tank valve, V1, and the purge valve, V3. The lines upstream of V3 are used during the entire engine operating phases. The lines downstream of V3 are only used for purging. Valve V2 is the combustion chamber valve and is closed during chilldown. The purge nozzle expels the hot fluids into vacuum. A metal hose, marked as Flex, connects the stage lines to the engine lines. A filter is located at tank exit to avoid feed system pollution. At chilldown start, the tank volume is filled at 96.995%. The boxes indicate the locations of in-flight data acquisition. The indices ull , pi , B , ci , pvo and fo denote tank ullage, pump inflow, pump bearing, purge valve outflow and flex outflow, respectively. Chilldown is started when V1 is opened and V3 is continuously open.

5.2 Numerical System Model

Figure 3 (b) shows the numerical representation of the feeding system. The various components from figure 3 (a) can be easily identified but line L7 is divided into four parts to account for varying diameters. Each line consists of the fluid domain, the line wall and the insulation. The lines are discretized with 9 cells in axial direction. The line walls and the insulation layers are discretized with 10 cells in radial direction. The propellant tank is subject to heat fluxes, \dot{q}_l . These are chosen such that the flight data for p_{ull} is matched. An improved determination of \dot{q}_l is left to future studies. The tank walls are discretized with 5 cells in radial direction, 10 cells in longitudinal direction for the upper and lower domes and 1 cell in longitudinal direction for the cylinder. The liquid phase in the tank is discretized with 1 cell and the gas phase with 10 cells. Stratification in the liquid phase is hence neglected. The purge nozzle is discretized with 25 cells in axial direction. A further refinement of the grid leads to only negligible changes in the results. In this

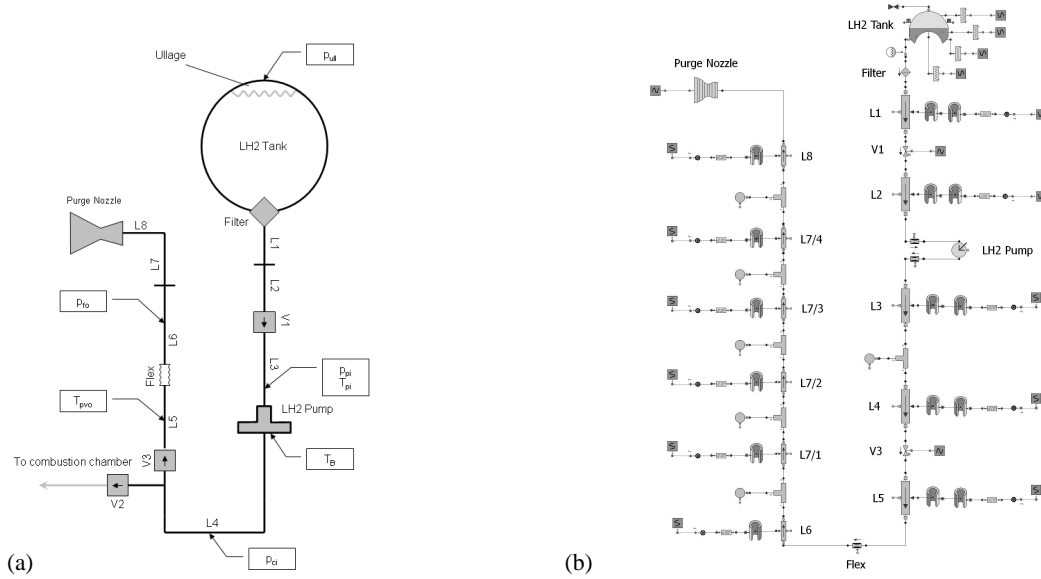


Figure 3: (a) schematic representation and (b) numerical model of the Ariane 5 ESC-A propellant feed system

sense, the present data can be assumed grid independent. The tank is initially pressurized with Helium in supercritical conditions at $T_{He} = 25K$. The initial temperatures of the tank walls correspond to the temperatures of the adjacent fluids. The ambient pressure is set to $p_{\infty} = 100Pa$, rather than vacuum, to avoid numerical problems due to icing. The flow conditions in the purge nozzle are critical and the flow is hence expelled from the system at supersonic velocities. The initial pressure in the system is set to $p_{init} = 1kPa$. The initial gas temperatures in the lines are set to the initial temperatures of the adjacent walls. The remaining initial and boundary conditions are discussed in section 6.2 below.

6. Validation Approach

6.1 Experimental Data

For each sensor from figure 3, data from 22 flights was collected. The data averages, $\bar{\phi}$, and their standard deviations, σ , can be used to define two limiting scenarios $\bar{\phi} \pm 3\sigma$. Assuming a Gaussian distribution, the probability that future flights produce data that lie within this bandwidth is 99.73%. In the following, all results are shown as a function of normalized time, $\tau = t/t_{CD}$, where t_{CD} is the total chilldown duration and $\tau = 0$ and $\tau = 1$ mark chilldown start and end, respectively. The latter is reached shortly after main stage (EPC) extinction and before ESC-A ignition. In practice, t_{CD} was varied for process optimization. However, the variations were small and the effect is largely averaged out.

6.2 Case Definition

Three numerical cases are considered and referred to as hot case, cold case and mean case. For the hot case, the initial feed system temperatures are high and p_{ull} is low. This leads to longer chilldown times. The case corresponds to $\bar{\phi} + 3\sigma$. The cold case corresponds to $\bar{\phi} - 3\sigma$. Here, the initial feed system temperatures are low and p_{ull} high. Finally, the mean case corresponds to $\bar{\phi}$. The initial conditions for these cases and the various system components are shown in table 3, where all values are normalized with the respective values for the mean case.

7. Results

Figures 4 (a)-(h) show the flight data and the present numerical results. $\bar{\phi}$ is represented by the solid black lines while $\bar{\phi} \pm 3\sigma$ are shown in solid grey. The cold case, the mean case and the hot case are represented by the black dashed lines, the black dashed-dotted lines and the black dotted lines, respectively, see also figure (h).

Table 3: Definiton of initial conditions, values are normalized with the mean case value

Value	Cold Case	Mean Case	Hot Case
$T_{1/2/3}$	0.8577	1	1.1423
$T_{4/5}$	0.9449	1	1.0551
T_6	0.8577	1	1.1423
T_7	0.8719	1	1.1281
T_8	0.8719	1	1.1281
T_B	0.8566	1	1.1434
T_{LH2}	0.9938	1	1.0042
T_∞	0.8816	1	1.1184
p_{ull}	1.0343	1	0.9657

Figure 4 (a) shows \tilde{p}_{ull} . The curves are quantitatively similar for the various cases and the global trends are captured. However, there are noticeable differences in the curve shapes. The numerical data show an initial rise, followed by a continuous drop, while the flight data initially oscillate around a constant mean before dropping. This is probably due to stage mechanical oscillations and transient evaporation processes in the feed system. The former cannot be accounted for in a straightforward manner in the present method while the latter are not entirely captured. This is because film boiling is neglected and phenomena like geyseyring are not represented. In reality, these effects have a non-negligible influence on system behavior by altering heat transfer rates and introducing transients. The discrepancies also suggests that \dot{q}_t is not entirely correct. While in reality $\dot{q}_t = \dot{q}_t(t)$, a constant value was prescribed here for simplicity. A more realistic prescription should improve predictions.

Figure 4 (b) shows \tilde{p}_{pi} . The general trends are similar to those observed for \tilde{p}_{ull} . However, the pressures here are notably higher than those in the ullage, which is due to the hydrostatic head. In addition, the absolute difference between the flight data and the numerical values is larger. This suggests that the computed stagnation pressure losses are overly optimistic. At $\tau \approx 0.98$, a significant drop in pressure can be observed. This marks the instant of EPC shut down. The acceleration then ceases and leads to a zero hydrostatic pressure component.

Figure 4 (c) shows \tilde{p}_{ci} . The numerical data is contained in $\bar{\phi} \pm 3\sigma$, which is contrary to the observations for \tilde{p}_{ull} and \tilde{p}_{pi} . The reason is that the sensitivity of the sensor is significantly lower. However, the results suggest that the numerical data is realistic.

Figure 4 (d) shows \tilde{p}_{fo} . As before, there are initial oscillations in the flight data that are subsequently damped out. For small τ , the numerical data is contained within $\bar{\phi} \pm 3\sigma$ values. However, for larger τ , the pressures temporarily exceed $\bar{\phi} + 3\sigma$, which suggests that not all relevant heat transfer mechanisms are captured. Accounting for film boiling might improve predictions. In addition, the fact that p_{ull} in the simulations is slightly higher than what is observed in flight contributes to the discrepancies. Interestingly, for storage temperatures close to T_{sat} (at p_{ull}), numerical tests show that the sudden increases in pressure are significantly smaller.

Figure 4 (e) shows Θ_{pi} . As for the pressures, an initial oscillatory behaviour can be observed in the experimental data. For later τ , the oscillations are damped out. The numerical data does not show this behaviour. This might partly be due to the fact that conduction in the pipe walls is ignored in the numerical model. A sudden drop in temperature can be observed at different τ for all data sets. For the cold case this drop occurs at $\tau = 0.35$, for the mean case at $\tau = 0.52$, for the hot case at $\tau = 0.75$ and for the experimental average at $\tau \approx 0.76$. The drops indicate the instant in time, τ_{DS} where the flow into the pump becomes desaturated. For $\tau > \tau_{DS}$, only liquid enters the pump. The prediction of τ_{DS} is hence important in order to avoid pump cavitation. The cold and the mean case are overly optimistic in this prediction while the hot case is close to the experimental values.

Figure 4 (f) shows Θ_B . The horizontal dashed line indicates the critical value, Θ_c . The curves for the experimental and the numerical data are qualitatively similar. However, some quantitative differences can be observed. For the flight data, Θ_c is reached at values τ of 0.60, 0.67 and 0.80 for $\bar{\phi} - \sigma$, $\bar{\phi}$ and $\bar{\phi} + \sigma$, respectively. For the cold case, the mean case and the hot case, the values (deviations) are 0.39 (-35%), 0.54 (-20%) and 0.71 (-12%), respectively. The numerical predictions are hence overly optimistic. This can be partly explained by the fact that film boiling is ignored. Accounting for it would lead to increased chilldown times due to reduced local heat transfer rates. In addition, the numerical tank ullage pressures are slightly higher than for the flight data. This entails higher mass flow rates and hence shorter chilldown durations. Finally, the mass and hence the thermal energy content of the pump might be underestimated with the simplified geometry from figure 1. However, the results suggest that the general trends are captured.

Figure 4 (g) shows Θ_{pvo} . As before, the general trends are reproduced well but the oscillations are missed. For

small τ , the numerical simulation predicts higher values for Θ_{pvo} than what can be observed in the experiment. This is because the sensor does not measure values $\Theta_{pvo} \gtrsim 0.36$. For larger t , the numerical cases are contained within $\bar{\phi} \pm 3\sigma$.

Figure 4 (h) shows the numerical results for $\Delta\dot{m}$. At EPC extinction, $\Delta\dot{m}$ is found to be 1.23, 1.00 and 0.78 for the cold case, mean case and hot case, respectively. In-house evaluations of flight data have determined the actual consumption as $\Delta\dot{m} = 0.83 \pm 0.12$. These are also indicated in the figure. The numerical results are hence conservative.

8. Summary and Conclusions

A simplified model to simulate the chilldown process for the hydrogen feeding system of a cryogenic rocket engine was presented. The approach is based on representing the fuel pump by a chilldown performance matrix. The latter is generated by a CFD analysis and then used in a systems simulation software. Comparisons of the numerical results with flight data were encouraging but showed that some of the details of system behavior are missed. Possible reasons for this include the neglect of film boiling, inadequate tank heat flux prescriptions and overly simplistic modeling of the pump geometry. These shortcomings should be addressed in future studies. Nevertheless, the proposed method has the following advantages: 1) The pump performance maps only have to be generated once; 2) Additional physical mechanisms can be implemented in a straightforward manner and the performance matrices expanded accordingly; 3) The running times are on the order of minutes or a few hours for the systems simulation. This is significantly lower than what would be required for a CFD simulation of the entire feeding system. 4) The approach provides conservative estimates for propellant consumption and realistic predictions of desaturation times.

9. Acknowledgements

This study was partly carried out under a research grant from the German Aerospace Center (DLR) within the framework of the SUCCESS improvement program. This support is gratefully acknowledged.

References

- [1] Davisson, J.C. and McHarris, G.A. 1971. S-IVB Restart Chilldown Experience. *J. Spacecraft* 8(2):99-104
- [2] Yuan, K. and Ji, Y. and Chung, J.N. 2009. Numerical modeling of a cryogenic chilldown process in terrestrial gravity and microgravity. *Int. J. Heat and Fluid Flow* 30:44-53
- [3] Yuan, K. and Ji, Y. and Chung, J.N. 2007. Cryogenic chilldown process under low flow rates. *Int. J. Heat and Mass Transfer* 50:4011-4022
- [4] Kawanami, O. and Azuma, H. and Ohta, H. 2007. Effect of gravity on cryogenic boiling heat transfer during tube quenching. *Int. J. Heat and Mass Transfer* 50:3490-3497
- [5] Kawanami, O. and Hiejima, T. and Azuma, H. and Ohta, H. 2003. Experimental study on cryogenic flow boiling under low gravity. *The 6th ASME-JSME Thermal Engineering Joint Conference*, TED-AJ03-361
- [6] Carey, V.P. 2008. *Liquid-Vapor Phase-Change Phenomena* - 2nd ed. Taylor & Francis.
- [7] Taitel, Y. and Dukler, A.E. 1976. A model for predicting flow regime transitions in horizontal and near horizontal gas-liquid flow. *AIChE* 22:47-55
- [8] Idel'cik, I.E. 1969. *Memento de pertes de charge - Coefficients de pertes de charge singulières et de pertes de charge par frottement*. Collection de la direction des études et recherches d'électricité de France. Eyrolles. Editeur Paris.
- [9] VDI Gesellschaft Verfahrenstechnik und Chemieingenieurwesen (Editor). 1997. *VDI Wärmeatlas. Band 8*. Springer-Verlag, Berlin Heidelberg.
- [10] Chen, J.C. 1966. Correlations for boiling heat transfer to saturated fluids in convective flow. *Eng. Chem. Proc. Design and Dev.* 5(3):531-535
- [11] Dougall, R.S., Rohsenow, W.M. 1963. *Film Boiling on the inside of vertical tubes with upward flow of the fluid at low qualities*. MIT Report No. 9079-26

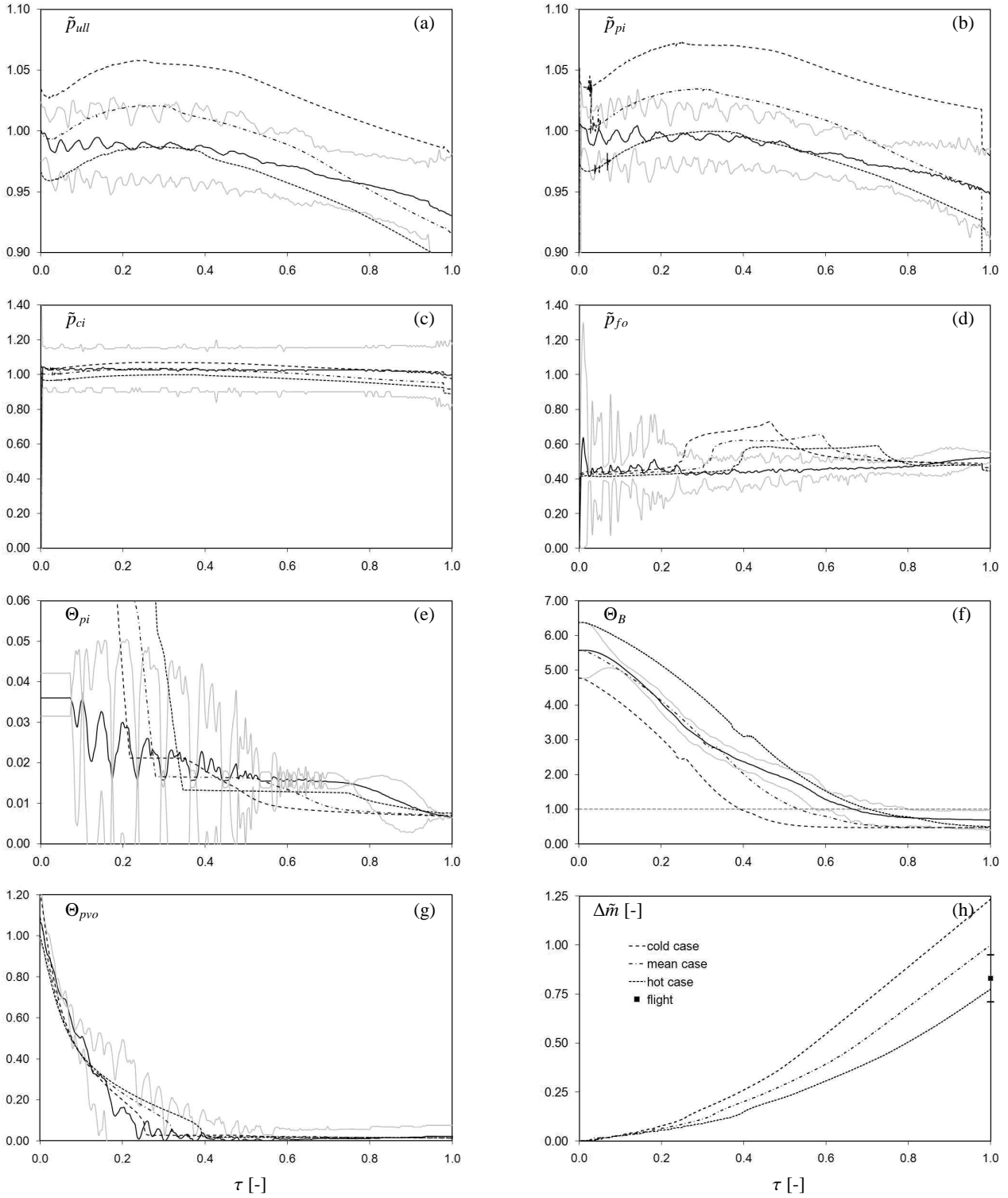


Figure 4: Comparison of numerical results with flight data: (a) \tilde{p}_{ull} ; (b) \tilde{p}_{pi} ; (c) \tilde{p}_{ci} ; (d) \tilde{p}_{fo} ; (e) Θ_{pi} ; (f) Θ_B ; (g) Θ_{pvo} ; (h) $\Delta \tilde{m}$; solid lines: $\bar{\phi}$; grey lines: $\bar{\phi} \pm \sigma$; cold case, mean case and hot case as shown in (h)